

# Quantum walks and correlated dynamics in an interacting synthetic Rydberg lattice

Tao Chen,<sup>1</sup> Chenxi Huang,<sup>1</sup> Bryce Gadway,<sup>1,2,\*</sup> and Jacob P. Covey<sup>1,†</sup>

<sup>1</sup>*Department of Physics, University of Illinois at Urbana-Champaign, Urbana, IL 61801-3080, USA*

<sup>2</sup>*Department of Physics, The Pennsylvania State University, University Park, Pennsylvania 16802, USA*

(Dated: April 2, 2024)

Coherent dynamics of interacting quantum particles plays a central role in the study of strongly correlated quantum matter and the pursuit of quantum information processors. Here, we present the state-space of interacting Rydberg atoms as a synthetic landscape on which to control and observe coherent and correlated dynamics. With full control of the coupling strengths and energy offsets between the pairs of sites in a nine-site synthetic lattice, we realize quantum walks, Bloch oscillations, and dynamics in an Escher-type “continuous staircase”. In the interacting regime, we observe correlated quantum walks, Bloch oscillations, and confinement of particle pairs. Additionally, we simultaneously tilt our lattice both up and down to achieve coherent pair oscillations. This work establishes synthetic Rydberg lattices of interacting atom arrays as a promising platform for programmable quantum many-body dynamics with access to features that are difficult to realize in real-space lattices.

Quantum walks describe the propagation of quantum particles on periodic potentials, and are the quantum mechanical analog of classical random walks. They play an important role in quantum simulation [1–3], quantum search algorithms [4, 5], and even universal quantum computation [6, 7]. Moreover, quantum walks offer a way to benchmark the coherence and entanglement of interacting dynamics in programmable quantum devices [8]. Quantum walks have been studied with neutral atoms in optical lattices [9, 10], superconducting circuits [11], trapped ions [12, 13], photonics [14], and other platforms [15]. These systems have demonstrated coherent evolution over tens of sites, where the geometry of the walks are constrained by the geometry of the underlying physical systems. The addition of a potential energy gradient leads to the observation of Bloch oscillations (BOs) [9, 16, 17] in which the particles remain localized and undergo periodic oscillations within nearby sites.

Synthetic dimensions provide an alternative bottom-up approach for Hamiltonian engineering to explore quantum walks and coherent dynamics of quantum particles [18–27]. Instead of tunneling between real-space sites such as the anti-nodes of an optical lattice or the transmons in a superconducting circuit, the “particle” hops within the state space of a host quantum system. The hopping rates between each pair of sites in the synthetic dimension is controlled with a drive that couples the two states. The local energy offset depends on the detuning of that drive. This paradigm offers several new opportunities: First, the “connectivity” between each pair of sites is fully programmable, enabling an emergent geometry and even the addition of topological phases [22, 28]. Second, the energy landscape is also fully programmable, which allows for the addition of any disorder pattern, lattice tilts [24, 25], or non-Euclidean geometry such as in the Escher-type “impossible” continuous stairs [29].

Here we utilize the large state space of individual Ry-

dberg atoms to encode a synthetic lattice [23, 28, 30, 31] with nine sites. Tunneling amplitudes and energy offsets are controlled with “nearest neighbor” drives, while interactions between the particles arise from the Rydberg dipolar exchange. Starting with single particles, we demonstrate highly coherent quantum walks in a flat lattice, Bloch oscillations in a tilted lattice, and dynamics within an Escher-type “continuous staircase” with a periodic boundary condition (PBC). We then introduce interactions by preparing a pair of closely-spaced Rydberg atoms, where we study the interplay of interactions and lattice tilt on the dynamics. We observe that moderate interactions induce free transport by a breakdown of Stark localization [32], but that strong interactions lead to re-entrant localization. Finally, we explore the scenario where the lattice is tilted both up *and* down simultaneously, observing the Floquet control of correlated pair hopping. Straightforward upgrades to our system could increase the state space and tunneling rates by an order of magnitude, enable two-dimensional geometries, and extend to hundreds of atoms. This work demonstrates the coherence and programmability of the Rydberg atom state space as a new platform for quantum simulation, quantum search algorithms, and even universal quantum computing.

*Single particle dynamics.*— Our synthetic lattice is routinely implemented in a probabilistically loaded one-dimensional tweezer array of single <sup>39</sup>K atoms with a series of dimerized trap configurations [28, 31, 33]. We postselect the singly loading in each trap dimer to observe the non-interacting single particle dynamics. The trapped atoms are globally excited to Rydberg state  $|0\rangle = |42S_{1/2}, m_J = 1/2\rangle$ . We then couple it to eight others – four on each side – with microwave drives [23, 28] such that the “particle” is initialized in the middle of the lattice chain [see Fig. 1(a)]. In this work, we primarily detect the initial Rydberg state,  $|0\rangle$ , or the state on one of the ends,  $|4\rangle$ , by mapping it back to the ground

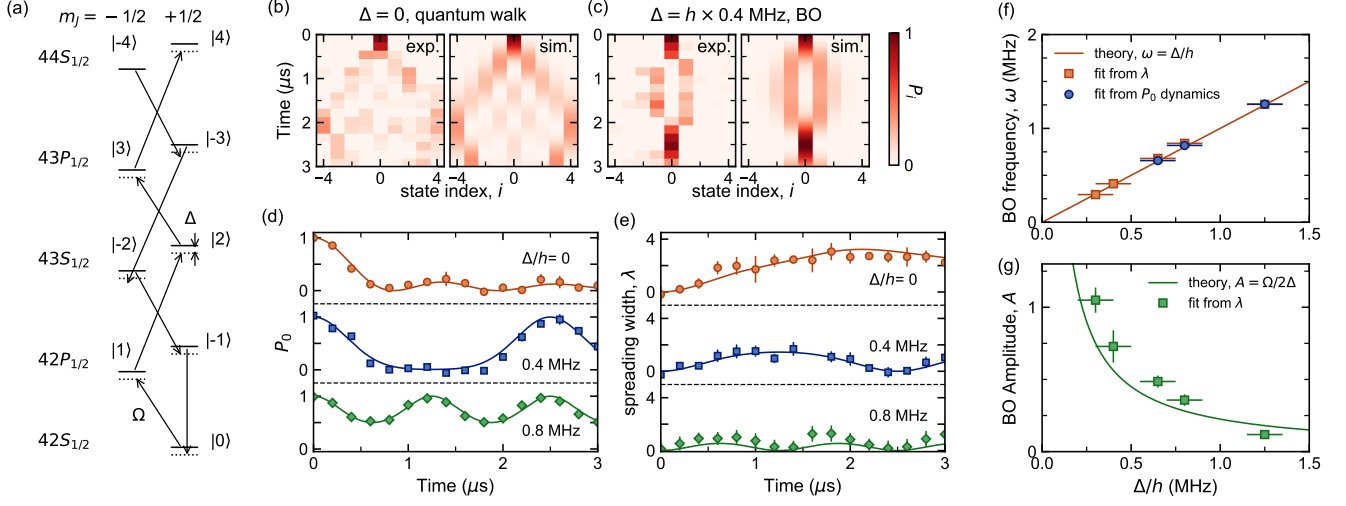


FIG. 1. **Bloch oscillations in a synthetic Rydberg state lattice.** (a) Level structure used to implement a 9-site Rydberg state lattice. Each state pair is coupled by a corresponding microwave tone (black arrows) with a Rabi rate  $\Omega$  and a detuning of  $\Delta$ . (b,c) Quantum walk [(b),  $\Delta = 0$ ] and BO [(c),  $\Delta/h = 0.4(1)$  MHz] dynamics in a 9-site lattice with  $\Omega/h = 0.45(1)$  MHz. (d,e) Time evolution of the population in the initial  $|0\rangle$  state,  $P_0$ , and the wavepacket spreading width  $\lambda$  for different detunings (see text). (f,g) BO frequency  $\omega$  and amplitude  $A$  as functions of detuning  $\Delta$ . Solid lines indicate the theory predictions. The error bars in (d,e) relate to the standard error of multiple independent data sets. The vertical (horizontal) error bars in (f,g) relate to the standard error of the fits (uncertainty of the calibrated detunings).

state such that it is bright to subsequent fluorescence detection of the atom. However, we are also able to detect each site independently, which we use to track the full single-particle dynamics in the synthetic lattice. We note that our experimental data throughout has been re-scaled based on the known preparation and measurement errors [28, 31, 34].

We first investigate the effect of different tilts on the wavepacket spreading described by the one-atom Hamiltonian

$$H_{\text{sp}} = \Delta \sum_j j c_j^\dagger c_j + \frac{\Omega}{2} \sum_j (c_{j+1}^\dagger c_j + \text{h.c.}) \quad (1)$$

with the hopping rates  $\Omega/2$  between each adjacent state pair and the programmable on-site potential. Figures 1(b,c) track the time evolution of the populations in all nine sites, showing both experimental results and simulations, respectively for the flat lattice case ( $\Delta = 0$ ) and for a tilted lattice ( $\Delta/h = 0.4$  MHz;  $\Delta \approx \Omega$ ). Our observations highly agree with the numerical simulations based on Eq.(1) with no free parameters. For the flat lattice case the wavepacket follows continuous-time quantum walk with reflections from the open boundaries, while in tilted lattice we see the breath-mode feature of the Bloch oscillation [9], i.e., the wavepacket primarily oscillates between the initial center site and nearby neighbors.

To further quantify our results and benchmark them against simulations, we plot in Fig. 1(d,e) both the center-site population,  $P_0$ , and the width of the wavepacket across the full lattice,  $\lambda = \sum_j |j| P_j$ , as a

function of time for three different  $\Delta$  values. We find excellent agreement with the simulations, including signatures of ballistic spreading and reflection for  $\Delta = 0$  and tilt-dependent localized breathing dynamics. Finally, Figs. 1(f,g) show the amplitude and frequency of the Bloch oscillations as a function of the tilt  $\Delta$ . Fitting results with the measured wavepacket spreading width  $\lambda$  are consistent with the theoretical prediction  $\lambda(t) = A[1 - \cos(2\pi\omega t)]$ , with frequency  $\omega = \Delta/h$  and amplitude  $A = \Omega/(2\Delta)$ . For large  $\Delta$ , the oscillation frequency can also be resolved from the measured  $P_0$  dynamics, which we employ in the following to describe the oscillating behaviors of an interacting pair.

Next, we build a ring geometry with eight states under PBCs, again initializing in  $|0\rangle$ . As shown in Fig. 2(a), finite detunings lead to an Escher-type “continuous staircase” configuration [29], where the energy cost is always positive (negative) when moving clockwise (counterclockwise). The left panels in Figs. 2(b-e) illustrate simulations of the population dynamics for four different tilts up to  $\Delta = \Omega/2$ . When  $\Delta = 0$ , the particle delocalizes around the ring, with transient refocusing at the initial  $|0\rangle$  site and at the opposing  $|4\rangle$  site. As the step height of the continuous staircase grows, the quantum walks persist but the gradient disrupts the refocusing at site  $|4\rangle$ . By tracking the population in the initial state  $|0\rangle$  and the state  $|4\rangle$  on the opposite side [right panels in Figs. 2(b-e)], we again find good agreement with simulations. We include simulations for the case with PBCs (matching the data) as well as the case in which sites  $|4\rangle$  and  $|-3\rangle$  are unconnected, corresponding to the open boundary

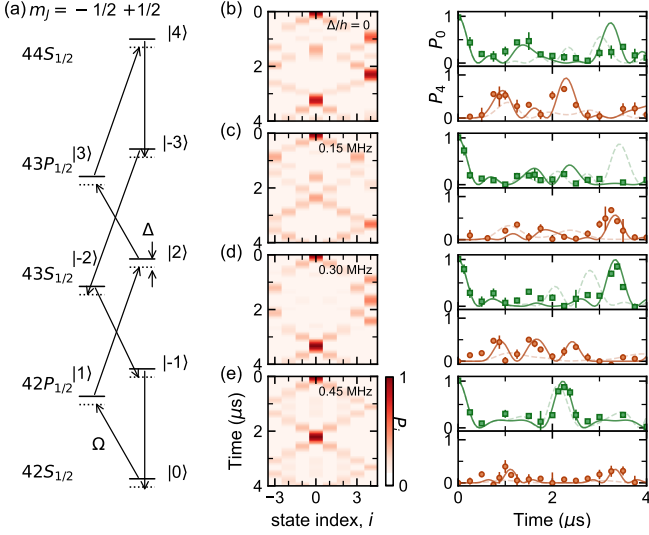


FIG. 2. **Dynamics for a non-interacting 8-site Rydberg lattice with Escher structure.** (a) State configuration to implement the continuous-staircase. Here we use  $\Omega/h = 0.90(2)$  MHz. (b-e) Left panels: simulated population dynamics for different detunings  $\Delta/h = \{0, 0.15, 0.30, 0.45\}$  MHz. Right panels: measured  $P_0$  (green squares) and  $P_4$  (orange circles) dynamics for corresponding detunings in left panels. Solid lines are the same simulations as those in the left panels, while the dashed lines, for comparison, indicate the population dynamics under open boundary condition by disconnecting the  $|4\rangle \rightarrow |-3\rangle$  transition. The error bars relate to the standard errors of multiple independent data sets.

conditions. When the tilt is small, such that the Bloch oscillation amplitude exceeds our finite system size, the two simulations are quite different, and the data agrees with the continuous staircase theory. However, for large tilt where the BO amplitude becomes small, the boundary conditions do not significantly impact the dynamics.

*Interacting atom pairs.*— We now discuss interacting dynamics and pair hopping by utilizing a pair of closely-spaced Rydberg atoms labelled as  $A$  and  $B$  with a spatial separation  $d_{AB}$ . The interacting Hamiltonian is

$$H_{\text{int}} = \sum_{i,j} V_{ij} c_{i,A}^\dagger c_{j,B}^\dagger c_{j,A} c_{i,B} + \text{h.c.}, \quad (2)$$

with  $V_{ij} \propto C_3^{ij}/d_{AB}^3$  for the dipolar exchange  $|i\rangle_A |j\rangle_B \leftrightarrow |j\rangle_A |i\rangle_B$ . We scale all  $V_{ij}$  to  $V = V_{0,-1}$  with the calculated  $C_3$  coefficients. In the experiment we vary the interaction strength by changing the tweezer separation  $d_{AB}$ . Here we return to the 9-state synthetic lattice in Fig. 1, and each atom also experiences the single-particle Hamiltonian (1). In our numerical simulations, the largely detuned state-changing interaction terms are excluded as we work in relatively weak interaction regime [34].

We consider the case of a highly tilted lattice with  $\Delta/h = 0.8(1)$  MHz. Figure 3(a) shows simulations of

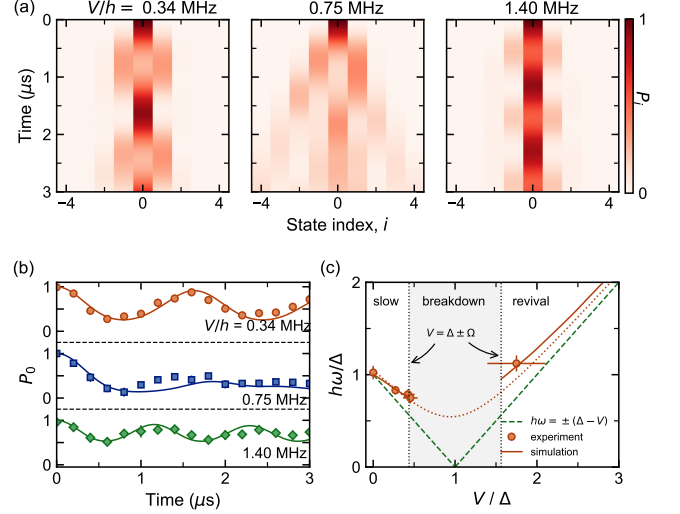


FIG. 3. **BO in an interacting atom pair.** (a) Simulated averaged population dynamics for atom pair in an interacting Rydberg state lattice under different interaction strength  $V/h = \{0.34, 0.75, 1.40\}$  MHz. (b) Time evolution of  $P_0$  under different interaction strength. Solid lines give the ideal numerical simulation results. The errorbars show the standard errors from multiple independent datasets. (c) Oscillation frequency  $\omega$  v.s. interaction-to-detuning ratio  $V/\Delta$ . With an increase of  $V/\Delta$ , the oscillation first slows down, then gets breakdown but finally revival. The boundaries of the breakdown region are determined by  $V = \Delta \pm \Omega$ . The solid line is obtained by fitting the numerically simulated ideal  $P_0$  dynamics. The dashed line with  $h\omega = \pm(\Delta - V)$  gives the energy gap between pair state  $|0, 0\rangle$  and triplets  $(|\pm 1, 0\rangle + |0, \pm 1\rangle)/\sqrt{2}$  in  $\Omega \rightarrow 0$  limit. The dotted line is the energy gap modified by finite small  $\Omega$  in formula  $h\omega \approx \sqrt{|\Delta - V|^2 + \Omega^2}$  for 3-state system  $\{|0\rangle, |\pm 1\rangle\}$  under interaction [34]. In experiment, we use  $\Delta/h = 0.8(1)$  MHz,  $\Omega/h = 0.45(1)$  MHz. The vertical (horizontal) errorbars come from fittings to the experimental datasets (uncertainties of both  $V$  and  $\Delta$ ).

the dynamics for three values of  $V$ , where the middle value corresponds to  $V \approx \Delta > \Omega$ . We expect to observe Bloch oscillations when  $V < \Delta$  and interaction-induced confinement when  $V > \Delta$ . In the intermediate regime where  $V \approx \Delta$ , we expect to observe delocalization in an anti-correlated quantum walk of the  $A$  and  $B$  atoms [34]. Our experimental results are consistent with these expectations. Here we use the dynamics of  $P_0 = (\langle c_{0,A}^\dagger c_{0,A} \otimes I_B \rangle + \langle I_A \otimes c_{0,B}^\dagger c_{0,B} \rangle)/2$  to describe the oscillation behaviors for interacting pairs; see Fig. 3(b). For both weak and strong  $V$ , we observe small-amplitude oscillations of  $P_0$ , with the frequency modified by the interaction. However, a damping feature without revival shows up when  $V \approx \Delta$ , indicating the breakdown of BOs.

Based on our observations, numerics, and energy arguments [34], we expect a “localization breakdown” region with interaction-induced transport for  $\Delta - \Omega < V < \Delta + \Omega$ . In the regions  $V < \Delta - \Omega$  and  $V > \Delta + \Omega$ , where we observe localization and clear oscillations of

$P_0$ , we quantify the agreement between theory and experiment by analyzing the oscillation frequency vs. the interaction strength. In these limits, we can relate this frequency to the energy gap between the  $|0,0\rangle$  and the  $(|\pm 1,0\rangle + |0,\pm 1\rangle)/\sqrt{2}$  triplet states. For  $\Omega \rightarrow 0$ , this is given by  $\pm(\Delta - V)$  [34]. Considering small but finite  $\Omega$ , the energy gaps of the truncated lattice ( $|-1\rangle$ ,  $|0\rangle$ , and  $|1\rangle$ ) are refined to  $\sim\sqrt{|\Delta - V|^2 + \Omega^2}$ . This latter form agrees well with our observations outside of the breakdown region. We note a slight deviation from the frequency based on numerics in the large  $V$  limit, which we attribute to the role of outer sites ( $|j| > 1$ ). Overall, these observations illustrate how correlated quantum walks and Bloch oscillations can be used to probe the effective band structure of the interacting system.

Finally, we explore a unique capability of synthetic lattices by simultaneously tilting the lattice both upward and downward. This scenario corresponds to a bichromatic drive with detunings  $\pm\Delta$  for each pair of states; see Fig. 4. We explore the interplay of this bichromatic drive and interactions  $V$  between the atoms when  $\Delta \approx 4\Omega$ . We start with a two-level system,  $|0\rangle$  and  $|1\rangle$ , as illustrated by the gray box in Fig. 4(a). In the non-interacting case, this corresponds simply to highly detuned Rabi dynamics, with a nearly static  $P_0 \approx 1$ . However, when interactions with strength  $V = 0.2\Delta$  are added, we observe large-amplitude pair oscillations between  $|0\rangle$  and  $|1\rangle$ . Measuring for different  $V$  values [see Fig. 4(c)], we find good agreement with the expected rate of activated pair hopping,  $\Omega_{\text{eff}} = 2|V|\Omega^2/|\Delta^2 - V^2|$ . We note that this activated pair-hopping [35] is controlled independently from the hopping of singles, and is thus distinct from the hopping of bound pairs in flat lattices ( $\Delta = 0$ ) when  $V \gg \Omega$  [9, 28, 36]. This process can also be viewed as the activation of “flip-flip” ( $\sigma^+\sigma^+$ ) and “flop-flop” ( $\sigma^-\sigma^-$ ) spin interactions [34], relevant for, e.g., the realization of Kitaev spin chains [37]. Lastly, this process is analogous to the recent Floquet activation [38] of Rydberg anti-blockade [39].

With this understanding of the bichromatic drives for the two-level system, we now return to the full nine-level system shown in Fig. 1(a), but with bichromatic drives. We measure the evolution of the  $|0,0\rangle$  population under different interaction strength  $V$ ; see Fig. 4(d). In the limit of zero interaction,  $P_{|0,0\rangle}$  remains high just as it did for the two-level case. As the interaction strength is increased, we find that  $P_{00}$  decays with an increasing rate. The measured dynamics are in good agreement with simulations, which suggest a coherent correlated delocalization that appears as a Gaussian decay on the short timescales probed in the experiment [34]. By fitting to the expected Gaussian decay  $e^{-\beta t^2}$ , we find the damping coefficient  $\beta$  agrees with the theory predicted scale as  $\sim V^2$  in weak interacting limit [34]; see Fig. 4(e).

*Concluding discussion.*— This work establishes synthetic Rydberg lattices in interacting atom arrays as a

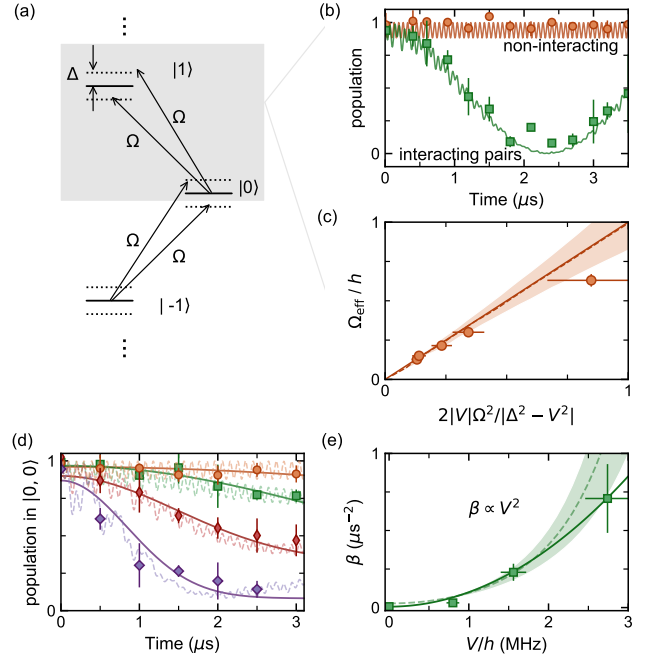


**FIG. 4. Pair hopping and pair dynamics under bichromatic driving.** (a) The driving scheme. Each Rydberg state pair is coupled by two equal strength ( $\Omega$ ) microwave tones, respectively detuned from resonance by  $\pm\Delta$ . In (b,c), we study only the two-state system of  $|0\rangle$  and  $|1\rangle$  (gray box) under a bichromatic drive. (b) Time evolution of the populations in  $|0\rangle$  for single atoms (orange circles) and  $|0,0\rangle$  for interacting pairs with  $V/h = -1.56(9)$  MHz (green squares). Here  $\Omega/h = 1.92(4)$  MHz and  $\Delta/h = 7.2(1)$  MHz. The solid lines are numerical simulations. (c) Comparison of the experimentally measured pair-hopping ( $|0,0\rangle \leftrightarrow |1,1\rangle$ ) rate  $\Omega_{\text{eff}}$  to the perturbation theory prediction (solid line). The dashed line shows the result from fittings to the numerically calculated  $P_{|0,0\rangle}$  dynamics. (d) Time evolution of the SPAM-corrected  $|0,0\rangle$  population for the 9-site lattice under bichromatic driving of each nearest-neighbor transition. The data plots, from top to bottom, relate to interactions  $V/h = \{0, 0.80(5), 1.56(9), 2.70(16)\}$  MHz with  $\Omega/h = 0.90(2)$  MHz and  $\Delta/h = 5.0(1)$  MHz. Solid lines are exponential fits  $P_{|0,0\rangle}(t) = a + b \exp(-\beta t^2)$  to the experimental data, while the dashed lines are numerical simulations. (e) The damping coefficient  $\beta$  vs. the interaction strength. The dashed line shows the fit of short-time numerics [dashed lines in (d)] to the same form. The solid line is a polynomial fit to the experimental data, showing the scale  $\beta \propto V^2$ . The shaded regions in (c,e) result from accounting for the known parameter uncertainties. The vertical error bars in (b,d) are standard errors from multiple independent measurements, while in (c,e) they give the standard errors of the fit. The horizontal errorbars in (c,e) reflect our uncertainties of the calibrated values of  $V$ ,  $\Omega$ , and  $\Delta$ .

promising platform to explore programmable quantum many-body dynamics. By studying quantum walks for single particles and correlated pairs, we demonstrate that the coherence of our system is comparable with that of other atomic platforms. Additionally, we leverage the



unique capabilities of synthetic dimensions to explore scenarios that are challenging to achieve with real dimensions, such as arbitrary energy landscapes, simultaneous tilting in two directions, and non-Euclidean geometry such as the Escher-type “continuous staircase.”

We note several straightforward ways to advance the coherence and increase the timescales of dynamics in this platform. First, it would be beneficial to implement trapping of our Rydberg states, either by blue-detuned bottlebeam traps [40] or with alkaline earth(-like) atoms with trappable ionic cores [41]. Second, a larger magnetic field would offer a larger spacing between the desired states and other Zeeman states, which would reduce unwanted off-resonant couplings and enable faster dynamics. Third, the use of higher Rydberg states or circular Rydberg states [42] – potentially even in a cryogenic environment [43] – would mitigate the effect of the finite Rydberg state lifetime. Already, this work sets the stage for complex many-body Rydberg dynamics with a large degree of programmability that can enable the study of few-body and many-body localized [44–48] and topological [49, 50] phases.

We thank Tabor Electronics greatly for the use of an arbitrary waveform generator demo unit. This material is based upon work supported by the National Science Foundation under grant No. 1945031 and the AFOSR MURI program under agreement number FA9550-22-1-0339.

---

\* bgadway@psu.edu

† jcovey@illinois.edu

- [1] M. Mohseni, P. Rebentrost, S. Lloyd, and A. Aspuru-Guzik, *The Journal of Chemical Physics* **129**, 174106 (2008).
- [2] M. B. Plenio and S. F. Huelga, *New Journal of Physics* **10**, 113019 (2008).
- [3] T. Kitagawa, M. S. Rudner, E. Berg, and E. Demler, *Phys. Rev. A* **82**, 033429 (2010).
- [4] A. M. Childs, R. Cleve, E. Deotto, E. Farhi, S. Gutmann, and D. A. Spielman, in *Proceedings of the Thirty-Fifth Annual ACM Symposium on Theory of Computing* (Association for Computing Machinery, New York, NY, USA, 2003) p. 59–68.
- [5] A. M. Childs and J. Goldstone, *Phys. Rev. A* **70**, 022314 (2004).
- [6] A. M. Childs, *Phys. Rev. Lett.* **102**, 180501 (2009).
- [7] S. E. Venegas-Andraca, *Quantum Information Processing* **11**, 1015 (2012).
- [8] D. K. Mark, J. Choi, A. L. Shaw, M. Endres, and S. Choi, *Phys. Rev. Lett.* **131**, 110601 (2023).
- [9] P. M. Preiss, R. Ma, M. E. Tai, A. Lukin, M. Rispoli, P. Zupancic, Y. Lahini, R. Islam, and M. Greiner, *Science* **347**, 1229 (2015).
- [10] A. W. Young, W. J. Eckner, N. Schine, A. M. Childs, and A. M. Kaufman, *Science* **377**, 885 (2022).
- [11] M. Gong, S. Wang, C. Zha, M.-C. Chen, H.-L. Huang, Y. Wu, Q. Zhu, Y. Zhao, S. Li, S. Guo, H. Qian, Y. Ye, F. Chen, C. Ying, J. Yu, D. Fan, D. Wu, H. Su, H. Deng, H. Rong, K. Zhang, S. Cao, J. Lin, Y. Xu, L. Sun, C. Guo, N. Li, F. Liang, V. M. Bastidas, K. Nemoto, W. J. Munro, Y.-H. Huo, C.-Y. Lu, C.-Z. Peng, X. Zhu, and J.-W. Pan, *Science* **372**, 948 (2021).
- [12] H. Schmitz, R. Matjeschk, C. Schneider, J. Glueckert, M. Enderlein, T. Huber, and T. Schaetz, *Phys. Rev. Lett.* **103**, 090504 (2009).
- [13] F. Zähringer, G. Kirchmair, R. Gerritsma, E. Solano, R. Blatt, and C. F. Roos, *Phys. Rev. Lett.* **104**, 100503 (2010).
- [14] A. Peruzzo, M. Lobino, J. C. F. Matthews, N. Matsuda, A. Politi, K. Poulios, X.-Q. Zhou, Y. Lahini, N. Ismail, K. Wörhoff, Y. Bromberg, Y. Silberberg, M. G. Thompson, and J. L. O’Brien, *Science* **329**, 1500 (2010).
- [15] J. Wang and K. Manouchehri, *Heidelberg, Springer Berlin* **10**, 978 (2013).
- [16] M. Ben Dahan, E. Peik, J. Reichel, Y. Castin, and C. Salomon, *Phys. Rev. Lett.* **76**, 4508 (1996).
- [17] Z. A. Geiger, K. M. Fujiwara, K. Singh, R. Senaratne, S. V. Rajagopal, M. Lipatov, T. Shimasaki, R. Driben, V. V. Konotop, T. Meier, and D. M. Weld, *Phys. Rev. Lett.* **120**, 213201 (2018).
- [18] M. Mancini, G. Pagano, G. Cappellini, L. Livi, M. Rider, J. Catani, C. Sias, P. Zoller, M. Inguscio, M. Dalmonte, and L. Fallani, *Science* **349**, 1510 (2015).
- [19] F. A. An, E. J. Meier, J. Ang’ong’a, and B. Gadway, *Phys. Rev. Lett.* **120**, 040407 (2018).
- [20] L. Yuan, Q. Lin, M. Xiao, and S. Fan, *Optica* **5**, 1396 (2018).
- [21] B. Sundar, M. Thibodeau, Z. Wang, B. Gadway, and K. R. A. Hazzard, *Phys. Rev. A* **99**, 013624 (2019).
- [22] T. Ozawa and H. M. Price, *Nature Reviews Physics* **1**, 349 (2019).
- [23] S. K. Kanungo, J. D. Whalen, Y. Lu, M. Yuan, S. Dasgupta, F. B. Dunning, K. R. A. Hazzard, and T. C. Killian, *Nature Communications* **13**, 972 (2022).
- [24] C. Oliver, A. Smith, T. Easton, G. Salerno, V. Guarrera, N. Goldman, G. Barontini, and H. M. Price, *Phys. Rev. Res.* **5**, 033001 (2023).
- [25] N. Englebert, N. Goldman, M. Erkintalo, N. Mostaan, S.-P. Gorza, F. Leo, and J. Fatome, *Nature Physics* **19**, 1014 (2023).
- [26] J. Deng, H. Dong, C. Zhang, Y. Wu, J. Yuan, X. Zhu, F. Jin, H. Li, Z. Wang, H. Cai, C. Song, H. Wang, J. Q. You, and D.-W. Wang, *Science* **378**, 966 (2022).
- [27] M. Parto, C. Leefmans, J. Williams, F. Nori, and A. Marandi, *Nature Communications* **14**, 1440 (2023).
- [28] T. Chen, C. Huang, I. Velkovsky, K. R. A. Hazzard, J. P. Covey, and B. Gadway, *Nature Communications* **15**, 2675 (2024).
- [29] E. J. Mueller, *Phys. Rev. A* **70**, 041603 (2004).
- [30] Y. Lu, C. Wang, S. K. Kanungo, S. Yoshida, F. B. Dunning, and T. C. Killian, *Phys. Rev. A* **109**, 032801 (2024).
- [31] T. Chen, C. Huang, I. Velkovsky, T. Ozawa, H. Price, J. P. Covey, and B. Gadway, Interaction-driven breakdown of aharonov–bohm caging in flat-band rydberg lattices (2024), [arXiv:2404.xxxxx](https://arxiv.org/abs/2404.xxxxx) [cond-mat.quant-gas].
- [32] E. E. Mendez, F. Agulló-Rueda, and J. M. Hong, *Phys. Rev. Lett.* **60**, 2426 (1988).
- [33] J. Ang’ong’a, C. Huang, J. P. Covey, and B. Gadway, *Phys. Rev. Res.* **4**, 013240 (2022).
- [34] See Supplementary Material for more experimental de-

tails and details on the theoretical formulation.

- [35] F. Meinert, M. J. Mark, K. Lauber, A. J. Daley, and H.-C. Nägerl, *Phys. Rev. Lett.* **116**, 205301 (2016).
- [36] K. Winkler, G. Thalhammer, F. Lang, R. Grimm, J. Hecker Denschlag, A. J. Daley, A. Kantian, H. P. Büchler, and P. Zoller, *Nature* **441**, 853 (2006).
- [37] H. Pan and S. Das Sarma, *Phys. Rev. B* **107**, 035440 (2023).
- [38] L. Zhao, M. D. K. Lee, M. M. Aliyu, and H. Loh, *Nature Communications* **14**, 7128 (2023).
- [39] C. Ates, T. Pohl, T. Pattard, and J. M. Rost, *Phys. Rev. Lett.* **98**, 023002 (2007).
- [40] D. Barredo, V. Lienhard, P. Scholl, S. de Léséleuc, T. Boulier, A. Browaeys, and T. Lahaye, *Phys. Rev. Lett.* **124**, 023201 (2020).
- [41] J. T. Wilson, S. Saskin, Y. Meng, S. Ma, R. Dilip, A. P. Burgers, and J. D. Thompson, *Phys. Rev. Lett.* **128**, 033201 (2022).
- [42] H. Wu, R. Richaud, J.-M. Raimond, M. Brune, and S. Gleyzes, *Phys. Rev. Lett.* **130**, 023202 (2023).
- [43] K.-N. Schymik, S. Pancaldi, F. Nogrette, D. Barredo, J. Paris, A. Browaeys, and T. Lahaye, *Phys. Rev. Appl.* **16**, 034013 (2021).
- [44] D. A. Abanin, E. Altman, I. Bloch, and M. Serbyn, *Rev. Mod. Phys.* **91**, 021001 (2019).
- [45] M. Schreiber, S. S. Hodgman, P. Bordia, H. P. Lüschen, M. H. Fischer, R. Vosk, E. Altman, U. Schneider, and I. Bloch, *Science* **349**, 842 (2015).
- [46] A. Lukin, M. Rispoli, R. Schittko, M. E. Tai, A. M. Kaufman, S. Choi, V. Khemani, J. Léonard, and M. Greiner, *Science* **364**, 256 (2019).
- [47] N. Y. Yao, C. R. Laumann, J. I. Cirac, M. D. Lukin, and J. E. Moore, *Phys. Rev. Lett.* **117**, 240601 (2016).
- [48] W. Morong, F. Liu, P. Becker, K. S. Collins, L. Feng, A. Kyprianidis, G. Pagano, T. You, A. V. Gorshkov, and C. Monroe, *Nature* **599**, 393 (2021).
- [49] S. Rachel, *Reports on Progress in Physics* **81**, 116501 (2018).
- [50] A.-S. Walter, Z. Zhu, M. Gächter, J. Minguzzi, S. Roschinski, K. Sandholzer, K. Viebahn, and T. Esslinger, *Nature Physics* **19**, 1471 (2023).

# Supplemental Material for “Quantum walks and correlated dynamics in an interacting synthetic Rydberg lattice”

## Calibration of the global flux for staircase lattice with $\Delta = 0$

The population dynamics strongly depend on the global flux in the 8-state ring structure with  $\Delta = 0$  in Fig. 2(a). Here we focus on the zero flux case. In the experiment, we adjust the phase  $\phi_{01}$  of the microwave frequency tone that drives  $|0\rangle \leftrightarrow |1\rangle$  transition (relative to the other tones, which all start with zero phase at the source) to achieve zero global flux. The calibration of the global flux and its dependence on  $\phi_{01}$  is based on the measured population dynamics of single atoms. Figure S1 shows the population in state  $|4\rangle$  after an evolution time of  $2.25 \mu\text{s}$  ( $\sim 2\hbar/\Omega$  with  $\Omega/\hbar = 0.90(2)$  MHz) for different  $\phi_{01}$ . Since we expect  $P_4$  to peak for zero global flux at  $t = 2\hbar/\Omega$ , we use  $\phi_{01} = 0.60(2)\pi$  (based on the simple Gaussian fit shown in Fig. S1) to achieve zero flux for all the measurements shown in Fig. 2 of the main text.

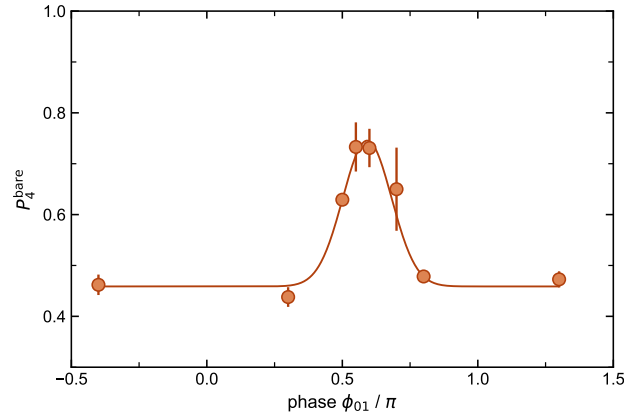


FIG. S1. **Calibration of the global flux for 8-state ring structure.** Measured population in state  $|4\rangle$ ,  $P_4$ , after an evolution time of  $2.25 \mu\text{s}$  under different values of the phase  $\phi_{01}$ . The solid line indicates the Gaussian fit to the data points. The error bars represent the standard errors from several independent measurements.

## Details of the interaction terms

As discussed in [28], two different dipolar exchange processes should be addressed in our setup: (i) resonant state-conserved flip-flop interactions for  $|i\rangle_A |j\rangle_B \leftrightarrow |j\rangle_A |i\rangle_B$ , (ii) non-resonant state-changing interactions for  $|i\rangle_A |j'\rangle_B \leftrightarrow |j\rangle_A |i'\rangle_B$  with a detuning  $\Delta_{ij}^{i'j'}$ . For the states employed to implement our synthetic lattice in Fig. 1(a), the smallest detuning  $|\Delta_{ij}^{i'j'}|_{\min} \sim \hbar \times 50$  MHz under the quantization  $B$ -field of  $\sim 27$  G. Since we work in the weak interaction regime with the maximum interaction strength  $V = \hbar \times 2.7$  MHz, i.e.,  $V \ll |\Delta_{ij}^{i'j'}|_{\min}$ , the non-resonant state-changing interaction terms have negligible effect on the pair dynamics and consequently can be safely excluded. In our numerical simulations, we directly use the flip-flop interacting Hamiltonian (2) in the main text. The interaction strength  $V_{ij} \propto C_3^{ij}/d_{AB}^3$  with  $d_{AB}$  the spatial separation of the atom pair. Similar to our previous work [28], we scale all  $V_{ij}$  to the calibrated value  $V = V_{0,-1}$  according to the relevant calculated  $C_3^{ij}$  coefficients, as listed in Table SI.

## Renormalization of the experimental measurements

As discussed in Ref. [28], the primary data we measure for the state population dynamics has a lower contrast as compared to the renormalized data presented in the main text. There are two main effects that reduce the contrast of the raw population dynamics data. First, the data typically features an average upper “ceiling” value  $P_u$ , which stems from inefficiency of STIRAP, as well as loss during release-and-recapture. There is also a lower baseline of the

$ i\rangle  j\rangle$	$C_3$	$ i\rangle  j\rangle$	$C_3$
$ 0\rangle  1\rangle$	-756.4		
$ 0\rangle  -1\rangle$	756.4		
$ 1\rangle  2\rangle$	-639.1	$ -1\rangle  2\rangle$	639.1
$ 1\rangle  -2\rangle$	639.1	$ -1\rangle  -2\rangle$	-639.1
$ 2\rangle  3\rangle$	-834.4	$ -2\rangle  3\rangle$	834.4
$ 2\rangle  -3\rangle$	834.4	$ -2\rangle  -3\rangle$	-834.4
$ 3\rangle  4\rangle$	-705.0	$ -3\rangle  4\rangle$	705.0
$ 3\rangle  -4\rangle$	705.0	$ -3\rangle  -4\rangle$	-705.0

TABLE SI. Calculated  $C_3$  coefficients (units of MHz  $\mu\text{m}^3$ ) for the resonant dipolar exchange interaction terms.

measurements, having an average value  $P_l$ , that we believe stems from the decay (and subsequent recapture) of the short-lived Rydberg states, which results in the non-depumped Rydberg states having some probability to appear bright to subsequent fluorescence detection. These infidelities limit the contrast of state population dynamics.

For the averaged population dynamics in non-interacting singles ( $P_i = \langle c_i^\dagger c_i \rangle$ ) and the interacting pairs [ $P_i = \frac{1}{2}(\langle c_{i,A}^\dagger c_{i,A} \otimes I_B \rangle + \langle I_A \otimes c_{i,B}^\dagger c_{i,B} \rangle)$ ], we renormalize the measured  $P_i^{\text{bare}}$  to  $P_i = (P_i^{\text{bare}} - P_l)/(P_u - P_l)$  with  $P_u = 0.93(1)$  and  $P_l = 0.32(1)$ . For the pair state dynamics, i.e.,  $P_{|0,0\rangle} = \langle c_{0,A}^\dagger c_{0,A} \otimes c_{0,B}^\dagger c_{0,B} \rangle$ , we renormalize with  $P_u = 0.86(1)$  and  $P_l = 0.32(1)$ . To note, when performing this normalization we systematically do not account for the statistical variations of the renormalization factors, which will lead to additional (and unaccounted for) uncertainties on the values of the renormalized population data.

### Determination of the oscillation frequency and breakdown region for atom pairs

Here we show how the interactions affect the oscillation frequency for atom pairs, and additionally we estimate the region in which interactions lead to a breakdown of localization effects. For large detunings, e.g.,  $\Delta > \Omega$  as used in Fig. 3 in the main text, the non-interacting Bloch oscillation is almost restricted to the center three sites. In this large-bias regime, the oscillation frequency is approximately equal to the energy gap between  $|0\rangle$  and  $|\pm 1\rangle$  under the dressed state picture. That is, when the dipolar exchange interaction is introduced, the atom pair in  $|0,0\rangle$  undergoes collective coupling to the neighboring triplet states (or superpositions of multiple triplets if we consider beyond the truncated  $|-1\rangle, |0\rangle, |1\rangle$  system). Then the oscillation frequency is determined by the energy gap between  $|0,0\rangle$  and

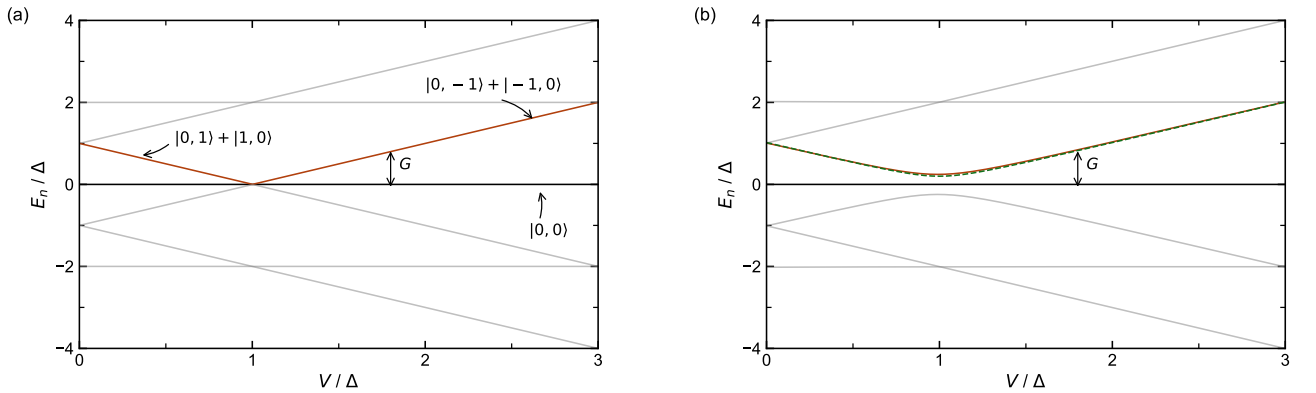


FIG. S2. **Eigenenergy distribution under different interaction strengths for the 3-state subsystem.** (a) With  $\Omega = 0$ , the zero energy band (solid black line) corresponds to the eigenstate  $|0,0\rangle$ . The eigenstate for the neighboring band (solid orange line) is the pair triplet:  $(|0,1\rangle + |1,0\rangle)/\sqrt{2}$  for  $V < \Delta$  and  $(|0,-1\rangle + |-1,0\rangle)/\sqrt{2}$  for  $V > \Delta$  (and vice-versa for the neighboring negative energy branch). The energy gap between the central bands is labelled as  $G = \pm(\Delta - V)$ . (b) For finite small  $\Omega/\Delta = 0.2$ , the central bands open up a gap at  $V/\Delta$ , corresponding to an eigenstate as a superposition of the  $|0,0\rangle$  state and pair triplets. The green dashed line indicates the approximated formula  $G = \sqrt{|V - \Delta|^2 + \Omega^2}$ . All gray lines in (a) and (b) correspond additional energy bands for this truncated system.



the neighboring eigenstates.

Instead of considering the whole 9-state system, we restrict ourselves to the 3-state subsystem,  $\{|0\rangle, |\pm 1\rangle\}$ , to get the approximate relation between the oscillation frequency and the energy gap. The Hamiltonian is

$$H = \pm\Delta |\pm 1\rangle \langle \pm 1| + \frac{\Omega}{2} (|0\rangle \langle \pm 1| + \text{h.c.}) + V_{0,\pm 1} (|0, \pm 1\rangle \langle \pm 1, 0| + \text{h.c.}) \quad (\text{S1})$$

with  $V_{0,\pm 1} = \mp V$ . We first consider the case with  $\Omega \rightarrow 0$ , for which the eigenenergy distribution under different interaction strengths is shown in Fig. S2(a). The initial  $|0, 0\rangle$  state is the eigenstate of the zero energy band, while the eigenstates for the neighboring bands with energy  $E_n = \pm(V - \Delta)$  are pair triplet states. The atom pair should in principle oscillate with a frequency given by the energy difference of the two bands, i.e.,  $G = \pm(V - \Delta)$  (although there would be zero amplitude of oscillation in the  $\Omega \rightarrow 0$  limit). This simple prediction relates to the dashed line shown in Fig. 3(c) of the main text. Small but finite  $\Omega$  introduces perturbations to the energy bands and opens up a gap at  $V/\Delta = 1$ ; see Fig. S2(b). Now the exact formula of the energy gap between the bands reads  $G = \frac{1}{2}\{10\Delta^2 - 4\Delta V + 2V^2 + 5\Omega^2 - [(6\Delta^2 + 4\Delta V - 2V^2 + \Omega^2)^2 + 8\Omega^2(3\Delta^2 - 10\Delta V + 3V^2 + \Omega^2)]^{1/2}\}^{1/2}$ . For small  $\Omega$ , we can neglect the second  $8\Omega^2$  term under the inner square root and get the approximated form

$$G \approx \sqrt{|\Delta - V|^2 + \Omega^2}, \quad (\text{S2})$$

as shown by the dotted line in Fig. 3(c) of the main text. We can see from Fig. S2(b) that this approximation works well.

Additionally, we can estimate the parameter region over which this approximated form should be invalid. Here we determine the breakdown boundaries of the localization and pair oscillations by letting the energy gap between the two bands be fully covered by the collective pair hopping rate, i.e.,

$$\sqrt{|\Delta - V|^2 + \Omega^2} = \sqrt{2}\Omega. \quad (\text{S3})$$

This leads to the simple relation  $V = \Delta \pm \Omega$ , shown as the two vertical dashed lines in Fig. 3(c) of the maintext. We also validate this formula from our numerical simulations, as the oscillatory fits to the  $P_0$  dynamics with collapse in this “breakdown” region.

### Time evolution of the atom-pair correlations

Figure S3 shows the time evolution of the atom-pair correlation  $C_{ij} = \langle c_{i,A}^\dagger c_{j,B}^\dagger c_{i,A} c_{j,B} \rangle$  for two of the quantum walk situations discussed in the main text - the case of two interacting particles hopping in a static, tilted lattice (the  $C_{ij}$  plots of Fig. S3(a), corresponding to the scenario explored in Fig. 3) and the case of two interacting particles hopping in a tilted lattice under bichromatic driving (the  $C_{ij}$  plots of Fig. S3(b), corresponding to the scenario explored in Fig. 4). In these two respective scenarios, the dynamics of the  $C_{ij}$  distributions reveal the anti-correlated and correlated nature of the hopping of the two particles (Rydberg electrons) in the synthetic dimension.

In the case of Fig. S3(a), the anti-correlated dynamics of the two interacting particles can be understood simply from a consideration of energy conservation. In this context, it is helpful to consider the  $C_{ij}$  graphs as plotting the density dynamics of pair states  $|i\rangle |j\rangle$  in an effective two-dimensional lattice. The energies of these pair states represent an effective potential landscape. In the case where atoms  $A$  and  $B$  both experience a tilted lattice, the effective pair state potential energy landscape has a gradient along the diagonal direction ( $i = j$ ), with lines of equal-energy states along the anti-diagonal ( $i = -j$ ). The single-particle hopping terms act separably as hopping in the  $i$  and  $j$  directions. In the absence of interactions, because of this separability of the Hamiltonian along  $i$  and  $j$ , the atoms independently experience Stark localization in the presence of a tilted lattice. Dipolar exchange interactions, having the form  $|i\rangle |j\rangle \leftrightarrow |j\rangle |i\rangle$ , introduce effective hopping in this two-dimensional pair-state lattice that is not separable along  $i$  and  $j$ . Thus, interactions between the atoms facilitate the breakdown of Stark localization, essentially allowing the atom pair states to delocalize along the resonant anti-diagonal channel. This pair state delocalization along the  $i = -j$  direction naturally leads to the buildup of anti-correlations. When the interactions  $V$  become sufficiently strong, pair dynamics along the resonant channel become disrupted. This suppression is also easy to understand: the initial  $|0\rangle |0\rangle$  state is only (by symmetry) connected to the triplet states  $(|-1\rangle |0\rangle + |0\rangle |-1\rangle)/\sqrt{2}$  and  $(|1\rangle |0\rangle + |0\rangle |1\rangle)/\sqrt{2}$ . Each of these states experiences a large interaction shift relative to the non-interacting  $|0\rangle |0\rangle$  state, such that direct dynamics are arrested for  $V \gg \Omega$ .

The dynamics seen in Fig. S3(b), under a strong lattice tilt and bichromatic driving, reveal a contrasting buildup of mostly positive (along the diagonal)  $C_{ij}$  correlations. This is consistent with the microscopic derivation and

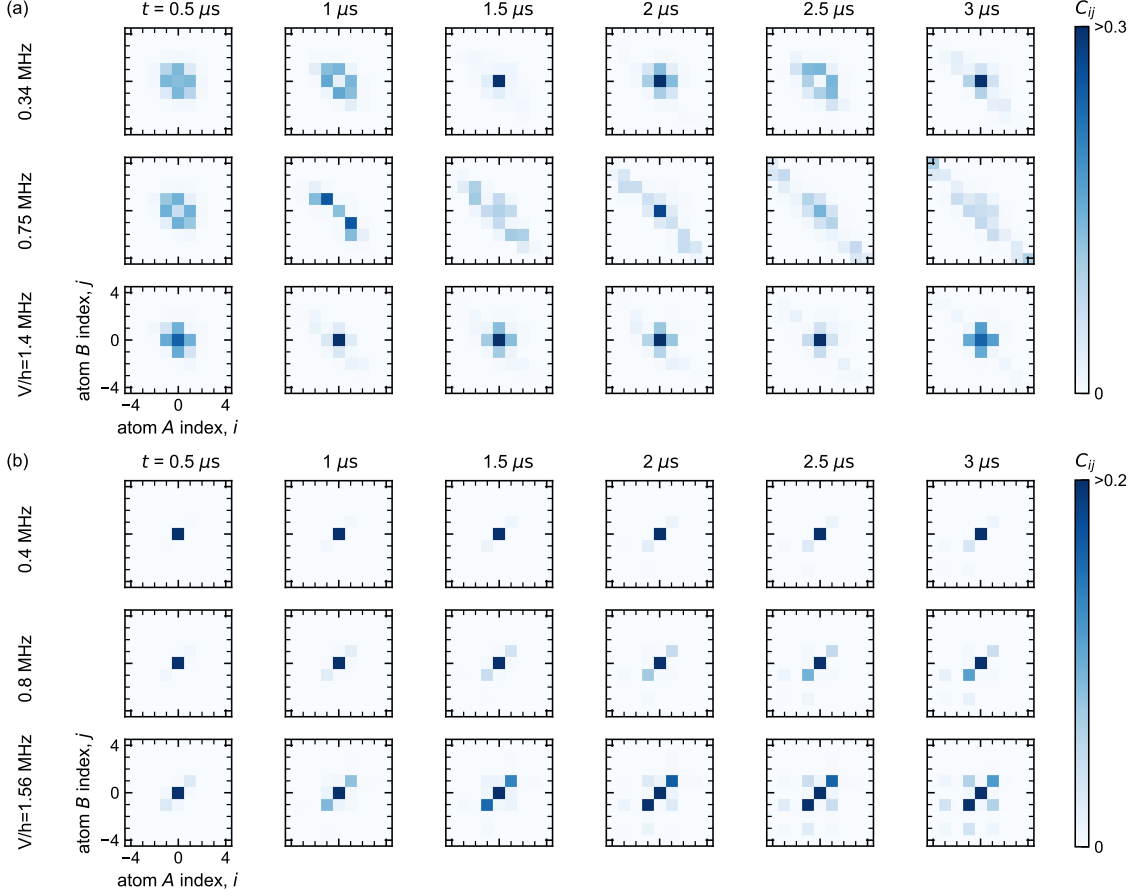


FIG. S3. **Numerically simulated time evolution of the atom pair correlations.** (a) Pair correlation  $C_{ij}$  after different evolution times  $t$  for the tilted 9-state lattice depicted in Fig. 1(a) of the main text [i.e., same conditions as in Fig. 3 of the main text]. Here  $\Delta/h = 0.8$  MHz and  $\Omega/h = 0.45$  MHz. (b) Pair correlation  $C_{ij}$  after different evolution times  $t$  for the 9-state lattice driven by bichromatic microwaves, as depicted in Fig. 4(a) of the main text. Here  $\Delta/h = 5.0$  MHz and  $\Omega/h = 0.90$  MHz.

description of activated pair-hopping (Eq. S4), and its generalization to the multi-state driven lattice. As can be seen in Fig. S3(b), the buildup of correlations is not purely along the diagonal. This imperfect correlation stems from the presence of additional processes (e.g.,  $|0\rangle|0\rangle \leftrightarrow |0\rangle|2\rangle$ ) as discussed below, which are allowed because of the equal  $\Delta$  values applied along adjacent links. As discussed below, such processes can in principle be suppressed, in which case one would expect purely positive (diagonal) correlations to build up in the strongly tilted and driven lattice.

#### Perturbation theory for the pair hopping rate in the bichromatic driving field

In large  $\Delta$  limit, i.e.,  $\Delta \gg \Omega, |V|$ , the pair oscillation  $|0,0\rangle \leftrightarrow |1,1\rangle$  under the bichromatic microwave field is activated by two resonant 2-photon transitions via the intermediate triplet state, as shown in Fig. S4. By directly applying second-order perturbation theory to the two processes, with the collective Rabi frequency  $\sqrt{2}\Omega$  and the single-photon detuning  $\Delta \pm |V|$  respectively, we have the effective Rabi frequency for the  $|0,0\rangle \leftrightarrow |1,1\rangle$  pair transition

$$\Omega_{\text{eff}} = \frac{(\sqrt{2}\Omega)^2}{2(\Delta - |V|)} + \frac{(\sqrt{2}\Omega)^2}{2(\Delta + |V|)} = \frac{2|V|\Omega^2}{\Delta^2 - V^2}. \quad (\text{S4})$$

This is the form used in Fig. 4(c). To note, the summed microwave phase of the two driving fields (both defined with the same real parameter  $\Omega$  in Fig. S4, but able to take controlled complex phases as well) can impart a controlled hopping phase for this correlated hopping process. And, as noted in the main text, this pair-hopping can be controlled entirely independently of the resonant hopping of individual atoms.

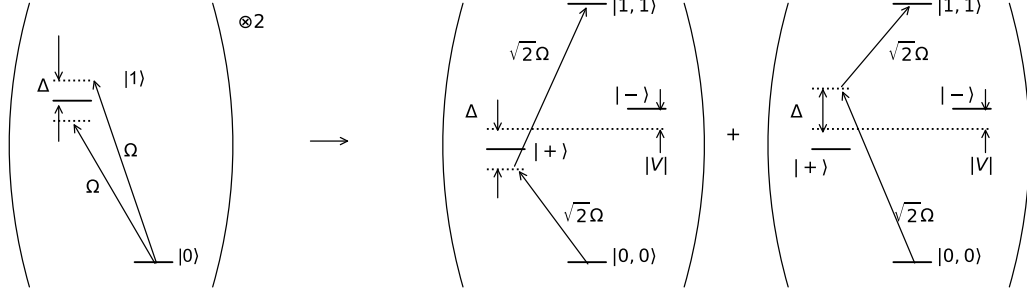


FIG. S4. **Decomposition of the pair hopping under the two-color microwave field into two 2-photon transitions that operate via the intermediate triplet state  $|+\rangle$ .** To note, the  $|-\rangle$  singlet state is decoupled from the initial  $|0,0\rangle \equiv |0\rangle|0\rangle$  state due to the symmetry of the global driving fields. The processes depicted at right are what give rise to the form of the effective pair-hopping term presented in Eq. S4.

When considering how this effective pair hopping rate generalizes when more states (beyond  $|0\rangle$  and  $|1\rangle$ ) are included (as in Fig. 4(d,e) of the main text), two effects become apparent. First, when all of the  $\Delta$  applied at the different transitions are set to be equal, additional resonant processes are in principle also allowed, such as  $|0\rangle|0\rangle \leftrightarrow |0\rangle|2\rangle$ . This type of process is responsible for the fact that the pair correlations that develop in Fig. S3(b) do not lie purely along the diagonal ( $i = j$ ). Second, one finds that, because the relevant exchange interactions  $V$  along different links vary along the synthetic dimension, and given the scaling of  $\Omega_{\text{eff}}$  with  $V$ , one expects that in general the pair hopping along a synthetic lattice will be quite non-uniform, and nearly disordered.

Importantly, the ability to control the parameters for each site-to-site link affords enough flexibility to both (1) suppress processes that are not of the form  $|i\rangle|i\rangle \leftrightarrow |i+1\rangle|i+1\rangle$  by setting unique (or simply staggered) values of  $\Delta$  and (2) compensate for non-uniformities of the  $V$  and  $\Delta$  values by locally controlling the  $\Omega$  terms to achieve uniform values of the  $\Omega_{\text{eff}}$  pair-hopping rates across each link.

#### Long time pair dynamics for the 9-state lattice under bichromatic driving with weak interactions

In our experiment on the 9-state lattice with each Rydberg state pair driven by a bichromatic field, we only measure the short time dynamics due to the short trap-release-recapture time window (less than 10  $\mu\text{s}$ ). Here we show in Fig. S5(a) the long-time dynamics from numerical simulations. In the weak interaction regime, the population in  $|0,0\rangle$  undergoes slow, but periodic oscillations with an oscillation frequency  $\omega$  that is nearly proportional to the interaction strength  $V$ ; see Fig. S5(b).

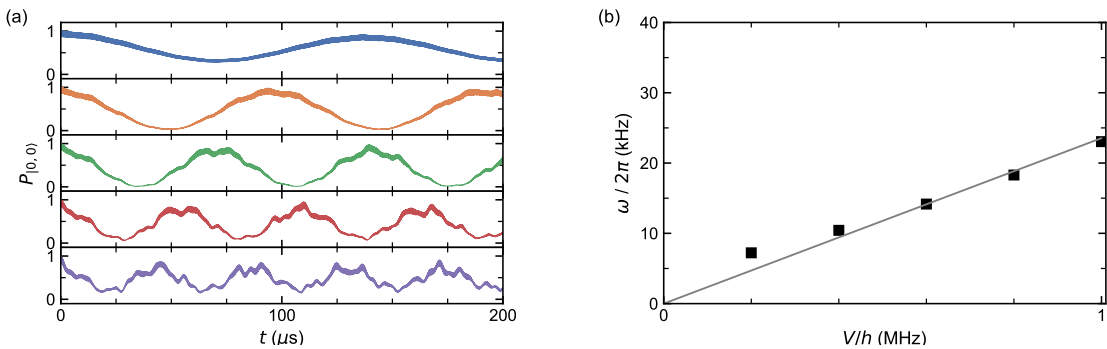


FIG. S5. **Long time  $P_{|0,0\rangle}$  dynamics for the 9-state lattice under bichromatic microwave fields.** (a) Numerically calculated time evolution of the population in  $|0,0\rangle$  in the 9-state lattice with the bichromatic driving scheme of Fig. 4(a) in the main text. From top to bottom, the interaction strengths are  $V/h = \{0.2, 0.4, 0.6, 0.8, 1.0\}$  MHz. Here we use  $\Omega/h = 0.90$  MHz and  $\Delta/h = 5.0$  MHz. (b) The fit-determined oscillation frequency of  $P_{|0,0\rangle}$ ,  $\omega$ , from fits to the dynamics in (a) with a cosine function  $P_{|0,0\rangle}(t) = a + \cos(\omega t)$ . The solid line shows the approximately linear relationship between the oscillation frequency and the interaction strength  $V$ .

On the short experimentally relevant timescales (over just a few  $\mu\text{s}$ ), where  $\omega t \rightarrow 0$  for kHz-scale  $\omega$ , we see that the relevant fitting function  $P_{|0,0\rangle} = a + b \cos(\omega t)$  can be approximated as  $(a - b) + 2b \exp(-\omega^2 t^2/4)$ . In the main text, we fit the short time dynamics with the formula  $P_{|0,0\rangle} = c + d e^{-\beta t^2}$ . By comparing these two forms, we see that  $\beta \sim \omega^2/4$ . Since  $\omega \propto V$ , we arrive at the simple approximated relationship  $\beta \propto V^2$ , as shown in Fig. 4(e) of the main text.